Available online at www.sciencedirect.com
SCIENCE DIRECT®
Journal of Photochemistry and Photobiology A: Chemistry 166 (2004) 19–31
Journal of Photochemistry and Photobiology A:Chemistry
www.elsevier.com/locate/jphotochem

Quantum dynamical simulations of ultrafast photoinduced electron-transfer processes

Dassia Egorova*, Wolfgang Domcke

Institute of Physical and Theoretical Chemistry, Technical University of Munich, Lichtenbergstr. 4 D-85748 Garching, Germany

Received 2 December 2003; received in revised form 6 January 2004; accepted 5 April 2004

Abstract

Multilevel Redfield theory is employed for the modeling of ultrafast electron-transfer (ET) reactions in polyatomic systems, exhibiting coherent wave-packet motion in excited and/or ground electronic states. Two-electronic-state models are constructed for excited-state ET driven by coherent vibrational motion in the initially excited donor state and characteristic features of ET dynamics in normal and inverted regions are outlined. Three-electronic-state models focus on the mechanisms of coherent repopulation of the electronic ground state, which may accompany ultrafast photoinduced ET. It is shown that wave-packet motion in the electronic ground state may be initialized not only by the laser excitation, but also by the reaction itself. Employing the numerically exact so-called self-consistent hybrid method, the validity of Redfield theory is critically examined.

Keywords: Electron transfer; Wave-packet dynamics; Redfield theory

1. Introduction

Being a fundamental phenomenon in chemistry, physics and biology, electron transfer (ET) has been attracting enormous attention of both experimentalists and theoreticians for many years. While thermal ET reactions have been investigated for decades, in recent years the attention has shifted towards photoinduced ET reactions occurring at subpicosecond time scales, so-called ultrafast ET processes [1]. Extensive experimental investigations of ET in the femtosecond regime have been performed, e.g., by Barbara and co-workers for betaines [2–6] and mixed valence compounds [7–10], and by Yoshihara and collaborators for various intermolecular reactions [11–15]. Observations of ultrafast ET processes also have been reported for bacterial photosynthetic reaction centers [16,17] and in numerous other systems [18–25].

An intriguing feature of many ultrafast ET reactions is the presence of oscillatory structures in time-resolved spectroscopic signals [1,9,10,16,18–23,26–28]. The quantum beats, which have been observed both in the ground and excited electronic states, reflect nonstationary wave-packet motion in underdamped vibrational modes. This suggests that vibrational motion may play an important role in ultrafast ET reactions.

The theoretical description of ET processes has traditionally been based on rate theories [29–31]. While such a description often is appropriate for thermally activated ET, the theoretical modeling of ultrafast photoinduced ET reactions generally requires a dynamical simulation of the reaction. To this end, a variety of methods have been proposed in recent years. There exist a few exact methodologies (such as the recently developed self-consistent hybrid method [32–35]), but most of the descriptions are approximate and thus limited to a certain parameter range. Among the approximate methods, multilevel Redfield theory has proven to be an efficient tool for modeling of ultrafast ET reactions which are driven by vibrational motion in a few strongly coupled reaction modes. In several applications, it has been shown to be well suited for studying the complex interplay of strong electronic coupling, coherent vibrational motion in high-frequency intramolecular quantum modes and dissipation due to a thermal environment [36–40].

Originally developed in the context of nuclear magnetic resonance [41], Redfield theory adopts a reduced density-matrix description of open systems [42–44]. This approach implies a separation of the problem into a relevant (system) part and an irrelevant (bath) part. The idea is to treat only the few degrees of freedom of the system explic-

* Corresponding author. Tel: +49 89 289 13618; fax: +49 89 289 13622.
E-mail address: egorova@ch.tum.de (D. Egorova).

1010-6030/$ – see front matter © 2004 Elsevier B.V. All rights reserved.
doi:10.1016/j.jphotochem.2004.04.034

itly, while all the others are traced out, being regarded as a dissipative environment. In Redfield theory, the elimination of the bath variables is achieved by a perturbative treatment of the system–bath interaction.

In applications of Redfield theory to ET reactions, the overall problem usually is partitioned in such a way that the system comprises the electronic states involved in the reaction as well as one or few reaction modes, while the remaining intramolecular and solvent degrees of freedom constitute the bath[1]. The perturbative treatment of the system–bath coupling is expected to be justified for ultrafast ET reactions, which are primarily driven by a few strongly coupled, but underdamped, high-frequency intramolecular modes.

The main advantage of multilevel Redfield theory is its simplicity and computational efficiency [36,37]. It has been widely applied to the modeling of ultrafast processes in condensed phases in the recent years [36–40,45–52]. The multilevel Redfield equation for the reduced density matrix has been numerically solved at different levels of accuracy, i.e., with or without additional simplifications, such as, e.g., the stationary Redfield-tensor approximation and the secular approximation. It has been shown that the secular approximation is not generally applicable for the modeling of ultrafast coherently driven ET [39], whereas the stationary Redfield-tensor approximation generally is quite accurate [40]. Applications to ET reactions with up to three reaction modes have been reported [39]. For systems of even larger size, further approximations within Redfield theory, such as the diabatic damping approximation [39,53], can be employed.

To explore the limits of applicability of multilevel Redfield theory, we have recently investigated the validity of the perturbative treatment of the system–bath interaction for ET models with various system, bath and system–bath coupling parameters [40]. Agreement between the multilevel Redfield-theory description and the numerically exact reference results (obtained with the self-consistent hybrid method [32–35]) has been established for small up to intermediate values of the system–bath coupling strength. Redfield theory has been found to perform particularly well at short time scales and for models of ET in the inverted region [40].

Here, we attempt to reveal the role of coherent vibrational motion in the ultrafast ET dynamics and focus on modeling of ultrafast ET reactions which exhibit coherent wave-packet motion in the excited and/or ground electronic states. The Redfield approach allows us to monitor and follow the wave-packet evolution in the electronic states of interest. The wave-packets are represented by the projection of the coordinate representation of the reduced density matrix on the corresponding electronic state. Two- and three-state models with a single reaction mode are considered.

It is well known that coherent vibrational motion may be created by femtosecond laser pulses in the excited electronic state as well as in the electronic ground state if there is a significant displacement between the equilibrium geometries of the optically coupled states. Hence, if reaction modes are Franck–Condon active, the ultrafast photoinduced ET is expected to be accompanied by coherent wave-packet motion.

To investigate the effects of this motion, we consider excited-state ET with nonstationary preparation of the initially excited donor state. The Franck–Condon-active reaction mode is coupled to the excited donor and acceptor states. The electronic ground state is not explicitly included in the system Hamiltonian (two-electronic-state models), but its location is taken into account by defining the shift between equilibrium geometries of the ground and donor states. We outline specific features of the dynamics in normal and inverted regions and demonstrate how nonstationary wave-packet motion in underdamped vibrational modes affects the reaction process. The transfer of vibrational coherences from the donor state to the acceptor state, which has been also investigated previously by Jean and Fleming [54], is illustrated by monitoring moving wave-packets.

On the other hand, there is experimental evidence of coherent repopulation of the electronic ground state during ET reactions [9,10,19,23,55]. Interestingly, ground-state vibrational motion also has been observed at frequencies which are not present in the excited-state dynamics. For example, femtosecond pump–probe experiments on plastocyanin [55] (photoinduced ligand-to-metal charge transfer) show that a low-frequency component, which is not observed in the resonance-Raman (RR) experiments on this system [56], is involved in the coherent recovery of the ground-state population. The RR inactivity of the mode suggests that there is no coordinate displacement between equilibrium geometries of the ground and initially excited electronic states along this coordinate. Hence, no moving wave packet can be prepared in the excited state and the coherent vibrational motion in the ground state cannot be induced by the laser excitation. However, if the equilibrium geometries of the ground and locally-excited electronic states coincide, vibrational coherence effects in the repopulation of the ground state can occur via one or several intermediate electronic states. In the case of the ET reaction in plastocyanin, this idea is supported by the experimental results of Fraga et al. [57] and Edington et al. [58], which suggest that the initial excited state decays via one or several lower-lying ligand-field states.

The three-electronic-state model calculations which we present here provide insight into coherent vibrational dynamics accompanying ultrafast photoinduced ET reactions, which occur via an intermediate state. The radiationless decay to the ground state is assumed to occur via a bridging charge-transfer state, which is nonadiabatically coupled to the locally-excited as well as to the ground state. Thus, the locally-excited and ground states are not coupled directly but through the charge-transfer state. This allows, in particular, to model the case of a Franck–Condon inactive reaction mode (stationary initial condition) and to observe the ground-state coherences of purely reactive origin, since no

[1] Redfield theory is referred to as “multilevel” if at least one vibrational degree of freedom is included in the system part [36].

wave-packet motion is generated in the initial locally-excited electronic state. A three-electronic-state model with nonstationary preparation also is considered. The presence of the intermediate charge-transfer state does not prevent the transfer of vibrational coherences to the ground state, but results in a certain delay in its repopulation.

Finally, we examine the quantitative accuracy of Redfield theory for two-electronic-state models by comparison with numerically exact reference results, obtained using the self-consistent hybrid method [32–35].

2. Model Hamiltonian

According to the system–bath separation scheme, the complete model Hamiltonian is written as the sum of a system and a bath Hamiltonian and a system–bath interaction operator:

$$H = H_{\mathrm{S}} + H_{\mathrm{B}} + H_{\mathrm{SB}}. \tag{1}$$

The system part is supposed to include electronic and vibrational degrees of freedom which are directly involved in the reaction. Adopting the diabatic representation for the electronic states [59–62], we define the explicitly treated system as

$$H_{\mathrm{S}} = \sum_i |\phi_i\rangle(h_i + \varepsilon_i)\langle\phi_i| + \sum_{i\neq j} |\phi_i\rangle V_{ij}\langle\phi_j|. \tag{2}$$

The diabatic states $|\phi_i\rangle$ are coupled to each other via electronic couplings V_{ij}, which allow for transitions between the states. We assume the electronic couplings V_{ij} to be constant (independent of the vibrational coordinates). ε_i are vertical electronic excitation energies and h_i denotes the vibrational Hamiltonian pertaining to the electronic state $|\phi_i\rangle$.

In the more general case of several (N) reaction modes, the vibrational Hamiltonian of state $|\phi_i\rangle$ can be written as a sum

$$h_i = \sum_q^N h_{iq}$$

of single-mode Hamiltonians h_{iq}. In this article, we restrict ourselves to the case of a single reaction mode and invoke the harmonic approximation for the vibrational motion[2].

The system vibrational Hamiltonians h_i are thus written as (hereafter $\hbar = 1$)

$$h_i = \frac{\omega_{\mathrm{S}}}{2}(P^2 + Q^2) + \kappa_i Q. \tag{3}$$

Here, Q denotes the dimensionless reaction coordinate and $P = -i(\partial/\partial Q)$ is the corresponding momentum operator. The vibrational frequency ω_{S} of the reaction mode is assumed to be the same for all electronic states. The parameters κ_i describe the electronic-vibrational coupling.

[2] For the study of anharmonic effects see, e.g., [63].

The system reaction mode is assumed to be linearly coupled to a bath of harmonic oscillators

$$H_{\mathrm{B}} = \sum_k \frac{\omega_k}{2}(p_k^2 + q_k^2), \tag{4}$$

$$H_{\mathrm{SB}} = Q\sum_k g_k q_k. \tag{5}$$

The bath frequencies, dimensionless coordinates and momentum operators are denoted as ω_k, q_k and p_k, respectively. The g_k describe the system–bath coupling strength. The parameters of the bath are characterized by its spectral function

$$J(\omega) = \frac{\pi}{2}\sum_k g_k^2\delta(\omega - \omega_k). \tag{6}$$

For the model calculations, we adopt the Ohmic spectral density [64]

$$J(\omega) = \eta\omega\,\mathrm{e}^{-\omega/\omega_{\mathrm{c}}}, \tag{7}$$

where η is a dimensionless parameter, characterizing the system–bath coupling strength, and ω_{c} is a bath characteristic frequency.

3. Multilevel Redfield theory

The Redfield equation for the reduced density matrix σ is obtained from the Nakajima-Zwanzig equation [65] employing the Born and Markov approximations in the description of dissipation as well as the system-eigenstate representation (see, e.g., [38,40] for details of the derivation of Eq. (8)):

$$\frac{\partial\sigma_{\mu\nu}(t)}{\partial t} = -i\omega_{\mu\nu}\sigma_{\mu\nu}(t) + \sum_{\kappa\lambda} R_{\mu\nu\kappa\lambda}\sigma_{\kappa\lambda}(t). \tag{8}$$

The basis states are defined via

$$H_{\mathrm{S}}|\mu\rangle = E_\mu|\mu\rangle, \tag{9}$$

and $\omega_{\mu\nu} = E_\mu - E_\nu$ are the system eigenfrequencies. The first term on the rhs of Eq. (8) accounts for the isolated-system dynamics, while the dissipation is described by the last term, i.e., by the Redfield tensor $R_{\mu\nu\kappa\lambda}$, which is usually written as

$$R_{\mu\nu\kappa\lambda} = \Gamma^+_{\lambda\nu\mu\kappa} + \Gamma_{\lambda\nu\mu\kappa} - \delta_{\nu\lambda}\sum_\alpha \Gamma^+_{\mu\alpha\alpha\kappa} - \delta_{\mu\kappa}\sum_\alpha \Gamma^-_{\lambda\alpha\alpha\nu}, \tag{10}$$

with

$$\Gamma^+_{\lambda\nu\mu\kappa} = \int_0^t \mathrm{d}\tau\,\mathrm{tr}_{\mathrm{B}}\{\langle\lambda|H_{\mathrm{SB}}(\tau)|\nu\rangle\langle\mu|H_{\mathrm{SB}}|\kappa\rangle\}\mathrm{e}^{-i\omega_{\mu\kappa}\tau},$$

$$\Gamma^-_{\lambda\nu\mu\kappa} = \int_0^t \mathrm{d}\tau\,\mathrm{tr}_{\mathrm{B}}\{\langle\lambda|H_{\mathrm{SB}}|\nu\rangle\langle\mu|H_{\mathrm{SB}}(\tau)|\kappa\rangle\}\mathrm{e}^{-i\omega_{\lambda\nu}\tau}, \tag{11}$$

where we have introduced

$$H_{\mathrm{SB}}(\tau) = \mathrm{e}^{iH_{\mathrm{B}}\tau}H_{\mathrm{SB}}\,\mathrm{e}^{-iH_{\mathrm{B}}\tau}.$$

The elements of the Redfield tensor, (11), are generally complex and time-dependent. In the following model calculations, we neglect the imaginary part of the Redfield tensor and employ the stationary Redfield-tensor approximation, that is, we extend the upper integration limit in (11) to infinity, $t \to \infty$.

4. Wave-packet dynamics during ultrafast ET

In this section, we present the results for ultrafast ET dynamics, obtained by solving the multilevel Redfield equation (Section 3) for two- and three-state models. Thus, the system part of the model Hamiltonian of Section 2 includes one reaction mode and two or three diabatic electronic states, respectively.

According to Eqs. (2) and (3), the diabatic potential-energy functions for the reaction coordinate are shifted parabolas. The electronic ground state is assumed to be located at the coordinate origin, $\kappa_G \equiv 0$. The coordinate displacements of the equilibrium geometry of the excited diabatic states from that of the electronic ground state are given by $-\kappa_i/\omega_S$.

Instantaneous excitation from the electronic ground state is assumed, i.e., at $t = 0$ a wave packet is prepared in the initially excited state at the equilibrium nuclear geometry of the electronic ground state.

The wave-packet dynamics is visualized as the time evolution of the coordinate representation of the reduced density matrix, projected on the relevant diabatic electronic states. The reduced density matrix (RDM) is numerically propagated by means of a fourth-order Runge–Kutta algorithm, adopted from [66]. The time-dependent population probabilities of the diabatic states,

$$P_i(t) = \mathrm{tr}\{\sigma(t)|\phi_i\rangle\langle\phi_i|\}, \tag{12}$$

are the relevant observables for ET dynamics and monitored as well. Converged results have been obtained using up to 20 system eigenstates for two-state models and up to 40 system eigenstates for three-state models.

The reaction-mode frequency is chosen as $\omega_S = 0.05$eV throughout the paper and so is the bath characteristic frequency, $\omega_c = \omega_S = 0.05$ eV. The system–bath coupling parameter η is varied in the considered models in order to obtain an effective damping of the vibrational motion on the time scale of interest. The temperature is set to zero, which accentuates quantum effects.

4.1. Ultrafast ET driven by wave-packet motion in the excited state

We consider ultrafast photoinduced excited-state ET, i.e., ET which occurs after a femtosecond laser excitation between two excited electronic states. The donor state (D) is optically coupled to the ground electronic state, and the acceptor state (A) is optically dark and nonadiabatically coupled to the donor state. Two diabatic electronic states are thus included in the system Hamiltonian, i =D, A in Eqs. (2) and (3).

4.1.1. ET in the normal region

To investigate the effects of coherent wave-packet motion in the normal regime, the following system parameters have been selected: The electron-vibrational couplings have been chosen as $\kappa_D = -2\omega_S = -0.1$ eV, $\kappa_A = -5.5\omega_S = -0.275$ eV and the vertical excitation energies of the donor and acceptor states differ by $\varepsilon_D - \varepsilon_A = 6.5625$ eV. A sufficient electron-vibrational coupling of the donor state κ_D ensures the preparation of a nonstationary initial state. The other parameters have been adjusted to obtain the respective geometry of the donor and acceptor potential-energy (PE) surfaces shown in Fig. 1. A moderate ET coupling ($V_{DA} = 0.01$eV) and weak damping ($\eta = 0.1$) have been chosen.

It is assumed that the initial state is given by a vibrational ground-state wave packet located at the origin of the vibrational coordinate ($Q = 0$) in the upper (donor) diabatic potential (shown by the arrow in the PE-surfaces graph). It can be seen that the mean energy of the wave packet lies above the energy of the crossing point of the diabatic potentials, that is, the crossing point is accessible for the moving wave packet.

Fig. 1 also shows the time-dependent population probability of the donor diabatic state, $P_D(t)$, and the time evolution of the reduced density matrix in the coordinate representation, projected on the donor, $\sigma_D(Q, t)$, and acceptor, $\sigma_A(Q, t)$, states. The wave-packet motion ($\sigma_D(Q, t)$, $\sigma_A(Q, t)$) is illustrated by three-dimensional (3D) and contour-plot views. The acceptor-state population probability is not shown, as it is trivially given by $1 - P_D(t)$.

The dotted-dashed curve in the population-probability graph of Fig. 1 gives the result for $P_D(t)$ without damping. The somewhat irregular beatings of the undamped system reflect so-called electronic coherences (low-frequency beatings) and vibrational effects (high-frequency beatings). The electronic coherences have often been observed in various dynamical simulations of ultrafast ET, but (to our knowledge) have not yet been detected experimentally. The frequency of these beatings depends on the electronic coupling V_{DA}. The quasi-periodic population dynamics of the undamped system demonstrates that there is no ET in the absence of damping.

The system dynamics including dissipation (solid line in the population-probability graph of Fig. 1) is electronically incoherent (the low-frequency oscillations disappear) and exhibits two different time scales: a fast initial step-like decay of $P_D(t)$ is followed by a much slower monotonous loss of the donor-state population.

The step structure, which has been observed in various model studies [39,40,48,49,67], reflects ET driven by coherent wave-packet motion: a fraction of the wave packet is transferred to the acceptor state each time the moving wave packet hits the crossing region. This interpretation is confirmed by the 3D and contour-plot graphs of $\sigma_D(Q, t)$: A

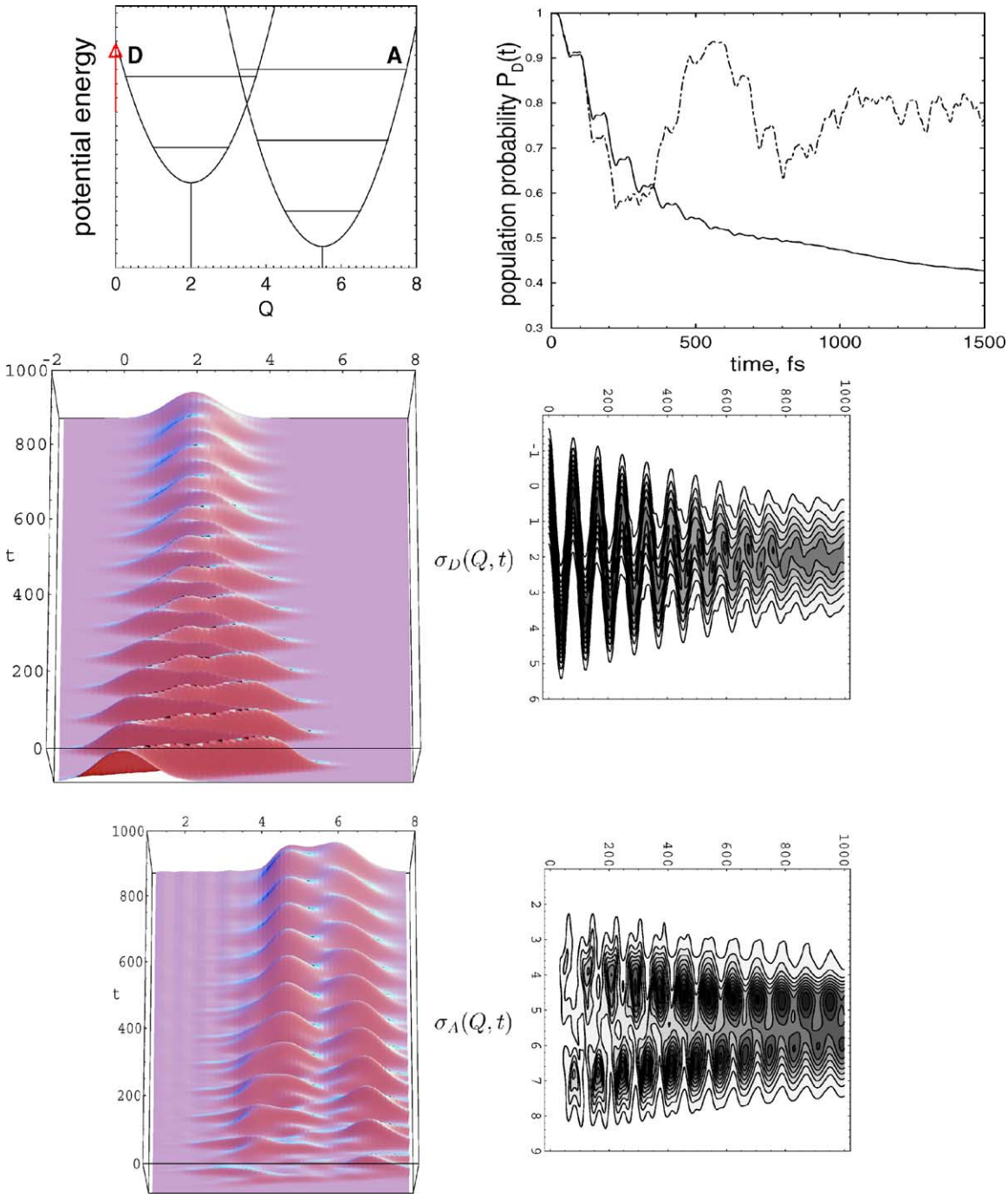

Fig. 1. Model for ultrafast excited-state ET in the normal region. Diabatic potential-energy surfaces (the zero-order vibrational states are indicated), population probability of the diabatic donor state, $P_D(t)$ (the dot-dashed curve represents the undamped, $\eta = 0$, system dynamics) and wave-packet motion in the donor, $\sigma_D(Q,t)$, and acceptor, $\sigma_A(Q,t)$, diabatic states (3D and contour plots).

Gaussian wave packet, prepared by instantaneous excitation from the ground electronic and vibrational state, is driven to the minimum of the donor potential ($Q = 2$) and its damped oscillations are clearly visible in 3D and contour-plot graphs. The wave-packet amplitude decreases because of the population transfer to the acceptor state.

The wave packet in the acceptor state ($\sigma_A(Q,t)$ in Fig. 1) appears in the vicinity of the crossing point of the diabatic potentials ($Q \simeq 3.5$) and oscillates towards the minimum of the acceptor potential ($Q = 5.5$), gaining the amplitude from the donor state and being damped at the same time scale as $\sigma_D(Q,t)$. The wave packets in the donor and acceptor states are out of phase, which leads to a double-peak structure of $\sigma_A(Q,t)$.

The vibrational wave-packet motion is quenched after ~600–800 fs due to vibrational relaxation. The wave

packet in the donor state relaxes to the ground vibrational state and the potential barrier prevents further ultrafast decay of the donor-state population. Instead, it exhibits monotonous decay due to tunneling (recall that the temperature is zero). This long-time dynamics is also reflected in the intensity gain/loss in the $\sigma_A(Q,t)/\sigma_D(Q,t)$ contour plots.

4.1.2. ET in the inverted region

To study ET dynamics in the inverted region (Fig. 2), we consider a model defined by the following system parameters: The electron-vibrational couplings are $\kappa_D = 2\omega_S = 0.1\,\text{eV}$, $\kappa_A = \omega_S = 0.05\,\text{eV}$, the vertical excitation-energy difference is $\varepsilon_D - \varepsilon_A = 0.175\,\text{eV}$, and the electronic coupling is $V_{DA} = 0.01\,\text{eV}$, as above. As in the previous section, a nonstationary initial preparation is assumed. At $t = 0$, a Gaussian wave packet of appropriate width is placed on the donor diabatic potential at the origin of the vibrational coordinate. It is seen already from the PE graph in Fig. 2, where the initial location of the wave packet is indicated by the arrow, that it will move periodically over the intersection point of the diabatic potentials. The initial excess in vibrational energy is more significant compared to Section 4.1.1, and a somewhat stronger system–bath interaction, $\eta = 0.3$, has been chosen. The diabatic PE curves, the population probability of the initially prepared donor state, $P_D(t)$, and 3D and contour-plot graphs of the wave-packets in both diabatic electronic states, $\sigma_D(Q,t)$, $\sigma_A(Q,t)$ are combined in Fig. 2 in the same manner as in the previous example.

The quasi-periodic dotted-dashed curve in the population-probability graph in Fig. 2 represents the dynamics of the undamped system ($\eta = 0$). It is similar to that of the normal region and reflects a superposition of electronic and vibrational oscillations. Inclusion of damping results in the population dynamics given by the full line. As in the normal region, the electronic coherences are quenched and we again observe ultrafast ET driven by coherent wave-packet motion, which manifests itself as the step-like decay of $P_D(t)$.

The initial vibrational amplitude of the donor-state wave packet, $\sigma_D(Q,t)$, is the same as in the normal region, but the oscillations are damped faster because of the stronger system–bath coupling. At ∼500 fs vibrational coherences in the donor state are quenched and the wave packet relaxes to the minimum of the corresponding potential ($Q = -2$). However, quasi-exponential decay at later times exhibits under-damped high-frequency oscillations. Since vibrational motion is efficiently damped after ∼500 fs, these modulations are probably of electronic origin and their frequency is determined by the energy gap between the donor and acceptor-state potentials [68].

In contrast to the previous example, ET is practically finished on the time scale of the vibrational relaxation. Even when the wave packet relaxes to the minimum of the donor potential the crossing point is accessible. Therefore, the population transfer is much more effective than in the normal-region example.

The transfer of vibrational coherences to the product state is illustrated by 3D and contour-plot graphs of $\sigma_A(Q,t)$ in Fig. 2. The wave-packet motion in the acceptor state is in phase with that in the donor state (constructive superposition). The damped oscillations, the gain in the intensity amplitude due to the ET and relaxation to the ground vibrational state are clearly visible. One can see that vibrational motion in the product state persists somewhat longer than in the donor state.

4.2. Coherent repopulation of the ground electronic state during ultrafast ET in the inverted region

So far, we have considered excited-state ET, the ground electronic state being excluded from the system dynamics. In this section, three-electronic-state models are considered to investigate the possibility of coherent ground-state formation in ET reactions that occur via an intermediate bridging state. The diabatic electronic states $|\phi_i\rangle$ which are included in the system Hamiltonian are the locally excited (LE) state, the intermediate charge-transfer (CT) state and the ground state (G), i.e., i = LE, CT, G in Eqs. (2) and (3). We consider two models representing stationary as well as nonstationary preparation (Sections 4.2.1 and 4.2.2, respectively).

4.2.1. Stationary preparation

In this section, we consider a Franck–Condon inactive reaction mode. A stationary wave packet is thus prepared in the initially excited electronic state. If coherent vibrational motion appears in the ground electronic state after the ET, it is not initiated by the laser excitation, but by the reaction itself.

The system parameters are defined in order to insure a fast and efficient transfer from the locally-excited to the intermediate CT state and then back to the ground state. The electron-vibrational coupling of the LE state is zero, $\kappa_{LE} = 0$, (stationary preparation) and that of the CT state is $\kappa_{CT} = 2\omega_S = 0.1\,\text{eV}$. The vertical excitation energies of the LE and CT states are equal, $\varepsilon_{LE} = \varepsilon_{CT} = 5\omega_S = 0.25\,\text{eV}$, so that there is no barrier between the LE and CT states and the barrier between CT and G states is very low (see the potential-energy surfaces in Fig. 3). The electronic couplings are rather substantial, comparable to the system frequency ($\omega_S = 0.05\,\text{eV}$): $V_{LE,CT} = 0.03\,\text{eV}$, $V_{CT,G} = 0.02\,\text{eV}$, and the system–bath coupling is determined by, $\eta = 0.15$. Fig. 3 shows the diabatic potentials for the system parameters chosen, the time-dependent population probabilities of the diabatic electronic states, $P_{LE}(t)$, $P_{CT}(t)$, $P_G(t)$, and the wave-packet motion in the CT and ground electronic states, $\sigma_{CT}(Q,t)$, $\sigma_G(Q,t)$, in three-dimensional (3D) and contour-plot representations. The LE-state projection of the RDM is not shown, as no wave-packet motion is created in this state due to the stationary initial condition.

The population probability of the LE state, $P_{LE}(t)$, exhibits electronic oscillations due to the nonadiabatic coupling $V_{LE,CT}$ which are damped on a time scale of about

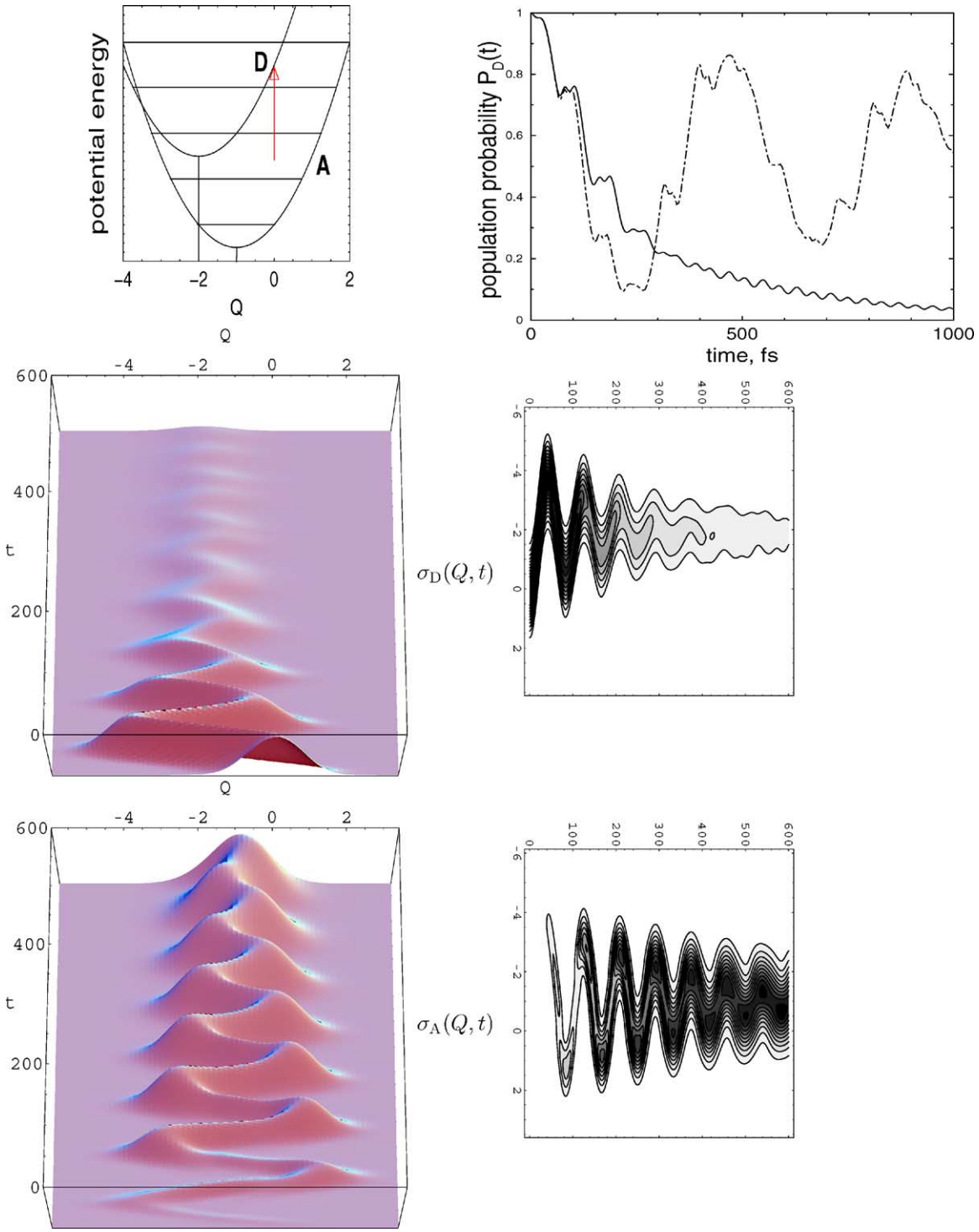

Fig. 2. Model for ultrafast excited-state ET in the inverted region. Diabatic potential-energy surfaces (the zero-order vibrational states are indicated), population probability of the diabatic donor state, $P_D(t)$ (the dot-dashed curve represents the undamped, $\eta = 0$, system dynamics) and wave-packet motion in the donor, $\sigma_D(Q,t)$, and acceptor, $\sigma_A(Q,t)$, diabatic states (3D and contour plots).

400 fs. The electronic coherences persist in the damped dynamics of the LE state due to a larger $V_{LE,CT}$ compared to V_{DA} of the models of Section 4.1. The higher-frequency modulations are absent since no vibrational motion is created in the LE state.

In the charge-transfer state population, $P_{CT}(t)$, a considerable gain is observed at $t \simeq 50$ fs. One can see electronic coherences at early times, which are then modulated by higher-frequency oscillations of vibrational origin reflecting the creation of the wave-packet motion in the CT state. The

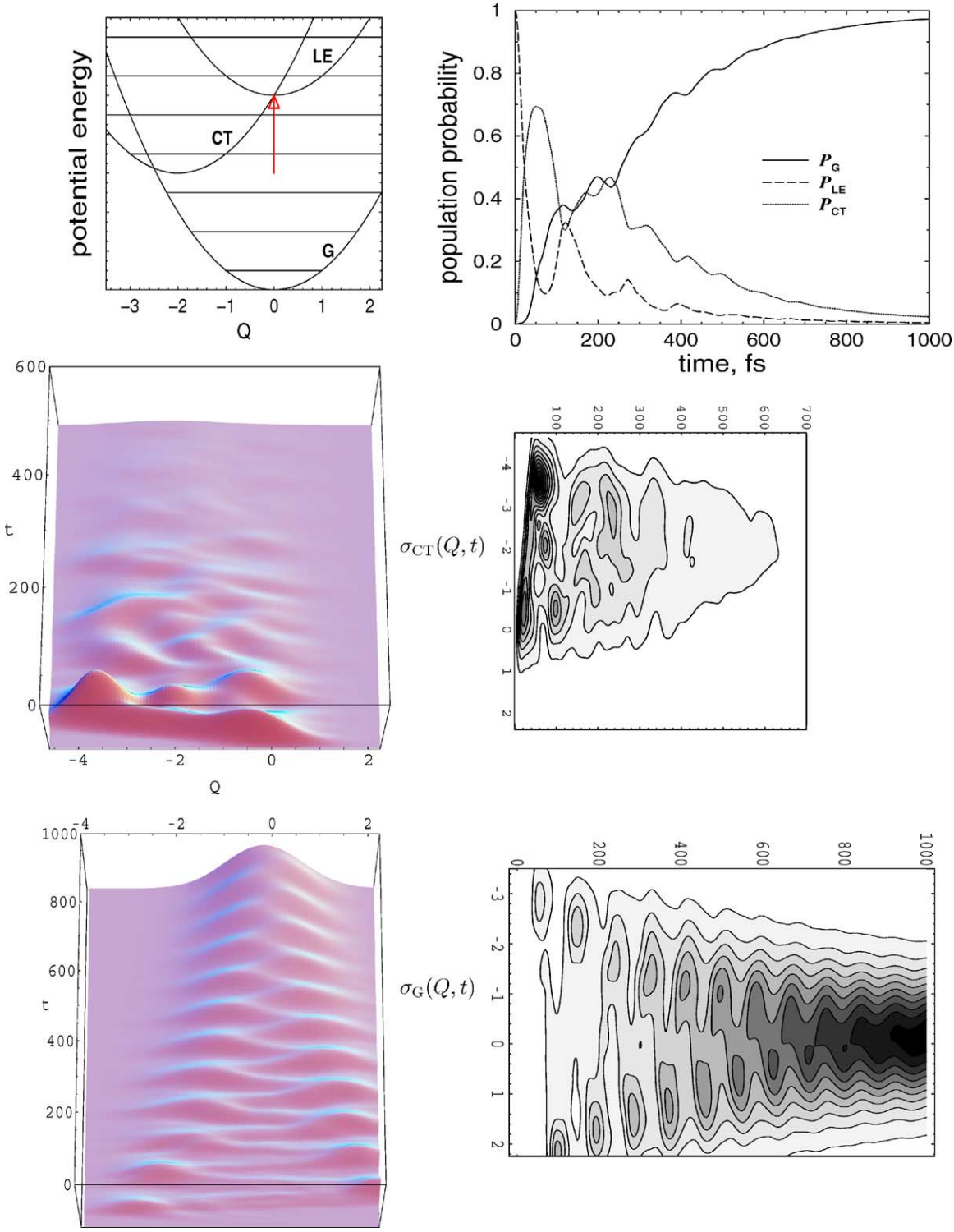

Fig. 3. Model for ultrafast ET with stationary preparation. Diabatic potential-energy surfaces (the zero-order vibrational states are indicated), population probabilities of the locally excited, $P_{LE}(t)$, charge-transfer, $P_{CT}(t)$, and ground, $P_G(t)$, electronic states, and wave-packet motion in the CT and G states, $\sigma_{CT}(Q,t)$, $\sigma_G(Q,t)$ (3D and contour plots), respectively.

familiar step structure can be recognized in the decay of the CT population between 200 and 600 fs. It reflects periodic vibrational motion in the CT state: The fast decay of $P_{CT}(t)$ occurs when the wave packet is localized in the vicinity of the crossing of the diabatic CT and G states, while the population remains constant when the wave packet is far from the crossing point. This interpretation is confirmed by the 3D and contour-plot graphs of the $\sigma_{CT}(Q,t)$. Appearing in the vicinity of the crossing point with the LE potential (at $Q=0$), the wave-packet in the CT state is strongly driven to the minimum of the corresponding potential ($Q=-2$), starts to moves periodically and disappears rapidly because of the back transfer to the ground state.

Despite the stationary preparation, pronounced coherent vibrational motion is observed in the ground electronic state ($\sigma_G(Q,t)$ in Fig. 3). It is reflected as step structure in the increase of the ground-state population, $P_G(t)$, and well seen in the 3D and contour plots of $\sigma_G(Q,t)$. The rather large initial amplitude of the oscillations is determined by the location of the crossing of the CT and ground-state diabatic potentials. The vibrational motion is damped due to the interaction with the bath modes and the system relaxes to the ground vibrational state within about 1 ps.

The model calculations demonstrate that coherent wave-packet motion in the ground state can be observed which is purely initiated by the reaction process. The experimental observation of coherent excitation of resonance-Raman inactive modes in the ground-state vibrational dynamics is an indicator that there must be at least three electronic states involved in a ET reaction.

The essential conditions for the occurrence of coherent ground-state vibrational motion due to electron transfer are: (i) substantial electron-vibrational coupling of the underdamped reaction mode in the intermediate CT state and, (ii) strong nonadiabatic coupling of this state to the LE and ground states.

4.2.2. Non-stationary preparation

In this section, we consider a three-state model with a nonstationary initial condition. The effects of nonstationary preparation for the excited-state ET have been considered in detail in Section 4.1. Here, we concentrate on the possible transfer of vibrational coherences created in the locally-excited state to the electronic ground state.

At $t=0$, a wave packet is placed on the diabatic potential of the locally-excited state at the origin of the vibrational coordinate. A nonequilibrium distribution is created due to the electron-vibrational coupling of the locally excited state, $\kappa_{LE}=2\omega_S=0.1$ eV. The electron-vibrational coupling of the charge-transfer state is $\kappa_{CT}=\omega_S=0.05$ eV and the vertical excitation energies are chosen as $\varepsilon_{LE}=5\omega_S=0.25$ eV, $\varepsilon_{CT}=1.5\omega_S=0.075$ eV. A moderate electronic coupling between the LE and CT states, as well as between the ground and CT states, has been chosen, $V_{LE,CT}=V_{CT,G}=\omega_S/5=0.01$eV, which appears to be sufficient for the effective transfer.

The nonstationary preparation results in an excess in vibrational energy and coherent vibrational motion in the initially prepared (LE) electronic state. To damp this initial vibrational coherence on a time scale of a few hundred fs, a stronger system–bath coupling than in the previously considered model (Section 4.2.1) is required. The system–bath interaction strength is thus set to $\eta=0.5$.

The diabatic potentials, the population probabilities of the three diabatic states, $P_{LE}(t)$, $P_{CT}(t)$, $P_G(t)$, as well as the projections of the coordinate representation of the RDM to these states, $\sigma_{LE}(Q,t)$, $\sigma_{CT}(Q,t)$, $\sigma_G(Q,t)$, are shown in Fig. 4. The coordinate/time scales of the graphs are the same.

The initial system evolution is characterized by a step-like decay of $P_{LE}(t)$ (dashed curve in the population-probability graph). Here, the step structure reflects coherent wave-packet motion in the LE electronic state. As is seen in the 3D and contour-plot graphs of $\sigma_{LE}(Q,t)$, the wave packet in the LE state exhibits damped vibrational motion with a loss of the population to the CT state. This motion is quenched after ∼400 fs due to vibrational relaxation. The crossing point is accessible even after the wave packet has relaxed to the minimum of the LE-state potential ($Q=-2$); a further monotonous decay of the LE-state population is thus observed. No electronic coherences are observed in the LE-state dynamics. The reason for this is a weaker electronic coupling and a stronger damping, compared to the model of Section 4.2.1.

The population dynamics of the CT state reflects a competition between the gain of population from the LE state and its loss to the ground electronic state. The population probability of this state, $P_{CT}(t)$ (dotted curve in the population-probability graph), increases up to ∼300 fs, but after this time the loss to the ground state is no longer compensated by the gain from the LE state. The wave-packet in the CT state, $\sigma_{CT}(Q,t)$, appears in the vicinity of the crossing point with the LE state and its periodical motion survives on approximately the same time scale as that in the LE state (see contour plots of $\sigma_{CT}(Q,t)$ and $\sigma_{LE}(Q,t)$). After relaxation to the minimum of the diabatic potential of the CT state, amplitude modulations of the wave packet can be recognized in the 3D and contour-plot graphs of $\sigma_{CT}(Q,t)$. In the population dynamics, they express themselves as the oscillatory structure of $P_{CT}(t)$ between ∼400 and ∼800 fs. These oscillations are probably of the same origin as those seen in the long-time dynamics of the donor state in the model of the excited-state ET in the inverted region ($P_D(t)$ in Fig. 2, Section 4.1.2). Here, they are due to the gap between the CT and ground-state potentials.

Coherent wave-packet motion in the ground state becomes visible at $t\simeq 100$ fs. The initial amplitude of the oscillations is determined by the location of the crossing of the ground state with the CT state and is slightly smaller than that in the LE and CT states. The oscillations are efficiently damped on a time scale of ∼400 fs, but small-amplitude vibrational motion survives up to ∼800 fs (see the contour plot of $\sigma_G(Q,t)$ in Fig. 4). The population probability of the

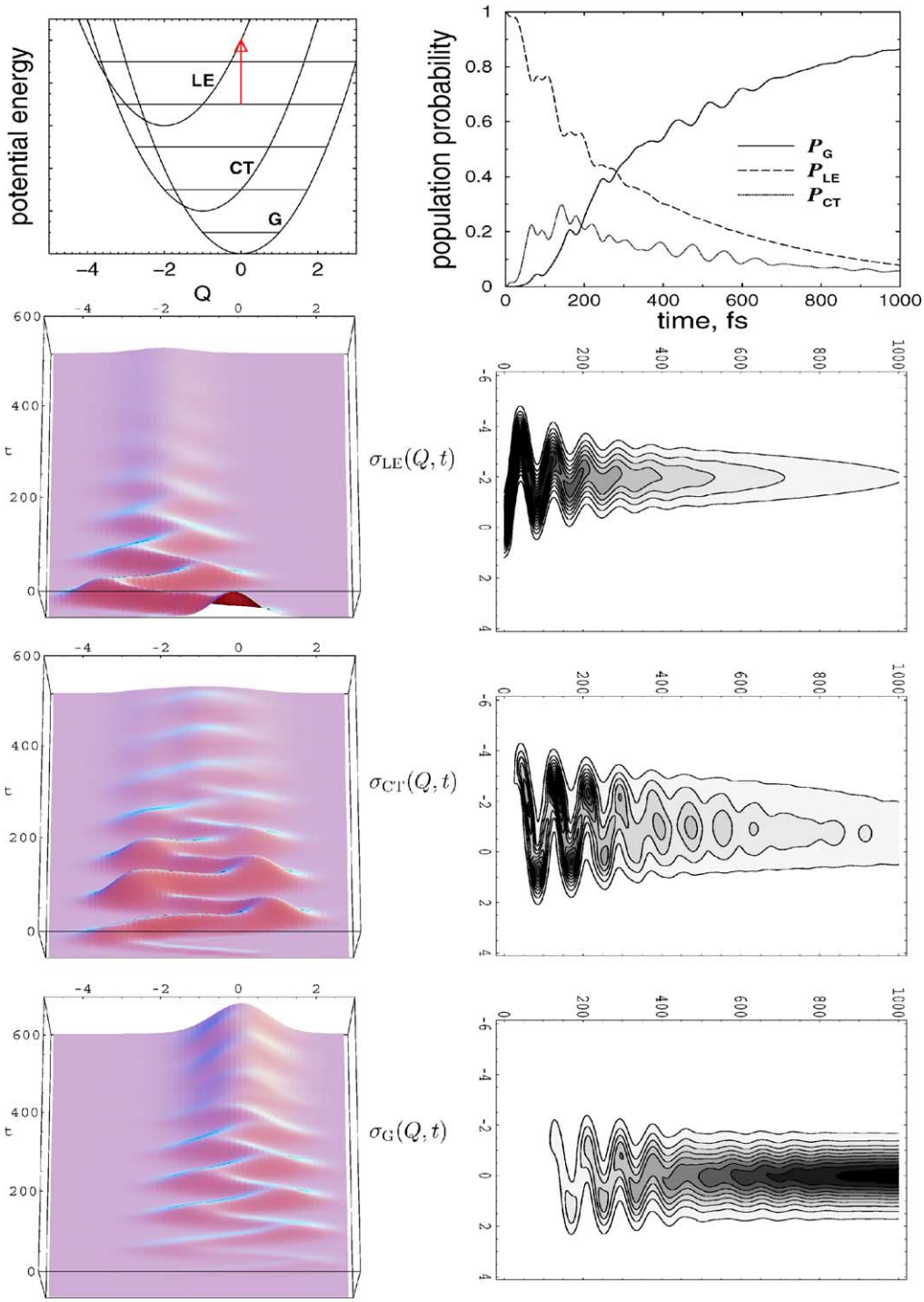

Fig. 4. Model for ultrafast ET with nonstationary preparation. Diabatic potential-energy surfaces (the zero-order vibrational states are indicated), population probabilities of the locally-excited, $P_{LE}(t)$, charge-transfer, $P_{CT}(t)$, and ground, $P_G(t)$, electronic states, and wave-packet motion in these states, $\sigma_{LE}(Q,t)$, $\sigma_{CT}(Q,t)$, $\sigma_G(Q,t)$ (3D and contour plots), respectively.

ground state, $P_G(t)$ (solid line in the population-probability graph), increases in a stepwise manner until ∼400 fs and exhibits oscillations which are a mirror image of the oscillations of $P_{CT}(t)$ between ∼400 and ∼800 fs.

The calculations demonstrate that the ET dynamics for this model is characterized by the consecutive transfer of the laser-induced coherent wave-packet motion from the locally-excited to the charge-transfer and then to the ground state. Coherent vibrational motion thus can survive several sequential nonadiabatic processes. It is conceivable that coherent vibrational dynamics can play an essential role in long-range ET via several bridge states, for example in

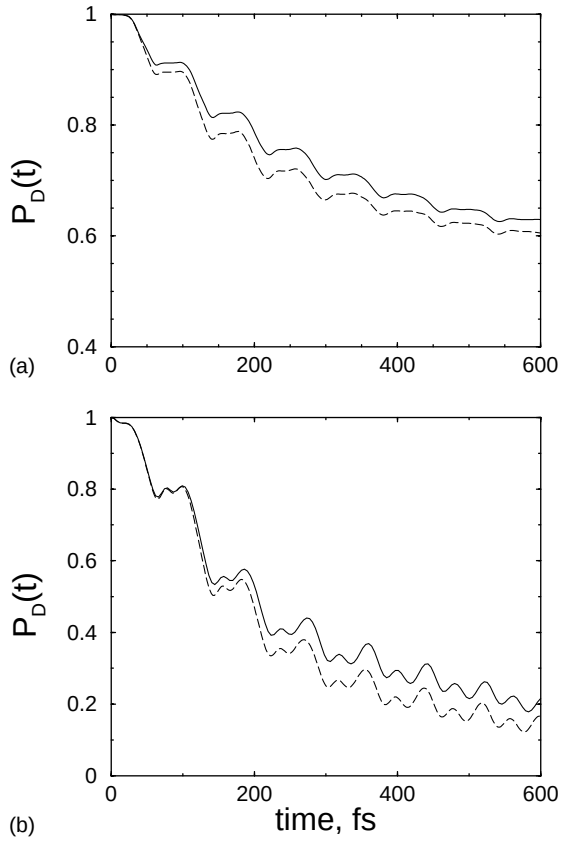

Fig. 5. Excited-state ET dynamics (population probability of the initially excited donor state) for: (a) normal and (b) inverted-region models. Shown are results of multilevel Redfield theory (dashed line) as well as results of the self-consistent hybrid approach (solid line).

photosynthetic reaction centers or in electronic transport through molecular wires.

5. Validity of multilevel Redfield theory for description of ultrafast ET processes

Here, we briefly inquire on the validity of Redfield theory for the description of ultrafast ET reactions. The results for the models considered in Section 4.1 are compared to predictions of numerically exact calculations within the self-consistent hybrid method[3].

The self-consistent hybrid method as well as its applications to different electron-transfer systems have been described in detail in [32–35]. Its basic idea is to introduce an iterative convergence procedure in a dynamical hybrid approach. While keeping its applicability to fairly general problems, the method aims at describing quantum dynamics for reactions in complex systems in a numerically exact way. To achieve this goal, the overall system is first partitioned into a *core* and a *reservoir*, based on any convenient, but otherwise rather arbitrary, initial guess. A dynamical hybrid calculation is then carried out, with the core treated via a numerically exact quantum mechanical method and the reservoir treated via a more approximate method. Next, the size of the core is systematically increased (and other variational parameters are adapted) until numerical convergence (usually to within 10% relative error) is reached for the overall quantum dynamics.

Fig. 5 shows the populational dynamics of the donor state for models of excited-state ET in the normal and inverted regions. Despite a slight discrepancy from the numerically-exact calculations, Redfield theory is capable to reproduce all the features of ET dynamics: the overall decay rate and the coherent structures are as those given by calculations within self-consistent hybrid method.

As has been shown in [40], the minor disagreement in the normal-region model (Fig. 5a) is due to the stationary Redfield-tensor approximation. The perturbative treatment of the system–bath interaction is fully justified in this regime ($\eta = 0.1$). On the other hand, in the case of the inverted-region model (Fig. 5b), the stationary Redfield-tensor approximation does not introduce any visible error (see [40] for details). The small difference from the self-consistent hybrid results is caused by the somewhat larger system–bath coupling strength, $\eta = 0.3$.

6. Conclusions

Multilevel Redfield theory has been employed for the modeling of ultrafast ET which exhibits vibrational wave-packet motion in the excited and/or ground electronic states. Two-state models for the excited-state ET in the normal and inverted regions, and three-state models for the ET in the inverted region have been considered.

In the two-state models, nonstationary initial conditions have been considered in order to create a moving wave-packet in the initially excited donor state. Wave-packet motion in the acceptor state, appearing during the reaction, has been detected both in the normal and inverted regions. The time scale of the damping of vibrational motion in the donor and acceptor states has been controlled by adjusting the system–bath coupling strength. In the normal region, two major time scales of ET have been observed: a very fast initial decay of the donor-state population due to coherent vibrational motion in this state and a much slower population transfer in the vibrationally relaxed system due to tunneling (zero temperature has been assumed). In the model describing ET in the inverted region, vibrational relaxation does not lead to a comparable slowing down of the reaction, due to the larger excess energy and the lower-lying crossing point of the diabatic potentials.

In the three-state models, we have employed multilevel Redfield theory to model ultrafast photoinduced ET reactions which occur in a stepwise manner via an intermediate CT state. Models with stationary and nonstationary

[3] The model Hamiltonian is as in [40].

preparation (i.e., with nonequilibrium and equilibrium nuclear geometry in the initial (LE) electronic state at $t = 0$) have been investigated. We have shown that if ET occurs via an intermediate charge-transfer state, coherent repopulation of the ground state is possible both with nonstationary and with stationary initial condition, i.e., regardless the Franck–Condon activity of the reaction mode, though the origin of the vibrational coherence is different.

The wave-packet dynamics with nonstationary initial condition is similar to that of the two-state model for the inverted region: an excess in vibrational energy and coherent vibrational motion is generated by nonstationary preparation. The coherent vibrational motion is gradually transfered from the initial LE state to the intermediate CT and then (after approximately 100 fs) to the ground electronic state.

On the other hand, no wave-packet motion is generated in the locally-excited state in the case of a Franck–Condon inactive reaction mode (stationary initial condition). However, a moving wave packet can be created in the the ground electronic state after its repopulation via the CT state.

While in the model with nonstationary initial condition the main effect of the CT bridge state is a certain delay in the repopulation of the ground state, the presence of at least one intermediate electronic state with strongly shifted equilibrium geometry is crucial for obtaining coherent vibrational dynamics in the product state in the case of stationary preparation. In this case, the vibrational coherence in the electronic ground state is generated by the ET reaction itself.

In order to justify the perturbative treatment of the system–bath interaction in the considered models, we have demonstrated that the predictions of multilevel Redfield theory are very close to numerically exact results obtained with the self-consistent hybrid approach.

Acknowledgements

We would like to cordially thank Michael Thoss and Haobin Wang for close and fruitful collaboration on exploring the validity of multilevel Redfield theory for description of ultrafast ET dynamics, which has resulted in [40]. Very special thanks to Michael Thoss for a careful reading of the manuscript.

References

[1] K. Yoshihara, K. Tominaga, Y. Nagasawa, Bull. Chem. Soc. Jpn. 68 (1995) 696.
[2] E. Åkesson, G.C. Walker, P.F. Barbara, J. Chem. Phys. 95 (1991) 4188.
[3] E. Åkesson, A.E. Johnson, N.E. Levinger, G.C. Walker, T.P. DuBruil, P.F. Barbara, J. Chem. Phys. 96 (1992) 7859.
[4] G.C. Walker, E. Åkesson, A.E. Johnson, N.E. Levinger, P.F. Barbara, J. Phys. Chem. 96 (1992) 3728.
[5] N.E. Levinger, A.E. Johnson, G.C. Walker, P.F. Barbara, Chem. Phys. Lett. 196 (1992) 159.
[6] A.E. Johnson, N.E. Levinger, W. Jarzeba, R.E. Schlief, P.F. Barbara, Chem. Phys. 176 (1993) 555.
[7] G.C. Walker, P.F. Barbara, S.K. Doorn, Y. Dong, J.T. Hupp, J. Phys. Chem. 95 (1991) 5712.
[8] K. Tominaga, D.A.V. Kilner, A.E. Johnson, N.E. Levinger, P.F. Barbara, J. Chem. Phys. 98 (1993) 1228.
[9] P. Kambhampati, D.H. Son, T.W. Kee, P.F. Barbara, J. Phys. Chem. A 104 (2000) 10637.
[10] D.H. Son, P. Kambhampati, T.W. Kee, P.F. Barbara, J. Phys. Chem. A 106 (2002) 4591.
[11] T. Kobayashi, Y. Takagi, H. Kandori, K.K.K. Yoshihara, Chem. Phys. Lett. 180 (1991) 416.
[12] H. Kandori, K.K.K. Yoshihara, J. Phys. Chem. 96 (1992) 8042.
[13] A.P. Yartsev, Y. Nagasawa, A. Douhal, K. Yoshihara, Chem. Phys. Lett. 207 (1993) 546.
[14] Y. Nagasawa, A.P. Yartsev, K. Tominaga, A.E. Johnson, K. Yoshihara, J. Chem. Phys. 101 (1994) 5717.
[15] Y. Nagasawa, A.P. Yartsev, K. Tominaga, B.P.B.A.E. Johnson, K. Yoshihara, J. Phys. Chem. 99 (1995) 653.
[16] M.H. Vos, J.C. Lambry, S.J. Robles, D.C. Youvan, J. Breton, J.L. Martin, Proc. Natl. Acad. Sci. U.S.A. 88 (1991) 8885.
[17] W. Zinth, P. Huppmann, T. Arlt, J. Wachtveitl, Philos. Trans. R. Soc. Lond. A 356 (1998) 465.
[18] K. Wynne, C. Galli, R.M. Hochstrasser, J. Chem. Phys. 100 (1994) 4797.
[19] K. Wynne, G.D. Reid, R.M. Hochstrasser, J. Chem. Phys. 105 (1996) 2287.
[20] I. Rubtsov, K. Yoshihara, J. Phys. Chem. A 101 (1997) 6138.
[21] I.V. Rubtsov, H. Shirota, K. Yoshihara, J. Phys. Chem. A 103 (1999) 1801.
[22] I. Rubtsov, K. Yoshihara, J. Phys. Chem. A 103 (1999) 10202.
[23] S. Engleitner, M. Seel, W. Zinth, J. Phys. Chem. 103 (1999) 3013.
[24] S.A. Kovalenko, R. Schanz, V.M. Farztdinov, H. Hennig, N.P. Ernsting, Chem. Phys. Lett. 323 (2000) 312.
[25] C. Zimmermann, F. Willig, S. Ramakrishna, B. Burfeindt, B. Pettinger, R. Eichberger, W. Storck, J. Phys. Chem. B 105 (2001) 9245.
[26] M.H. Vos, F. Rappaport, J.C. Lambry, J. Breton, J.L. Martin, Nature 363 (1993) 320.
[27] M. Seel, S. Engleitner, W. Zinth, Chem. Phys. Lett. 275 (1997) 363.
[28] B. Wolfseder, L. Seidner, G. Stock, W. Domcke, M. Seel, S. Engleitner, W. Zinth, Chem. Phys. 233 (1998) 323.
[29] N.R. Kestner, J. Logan, J. Jortner, J. Phys. Chem. 78 (1974) 2148.
[30] J. Jortner, M. Bixon, J. Chem. Phys. 88 (1988) 167.
[31] H. Sumi, R.A. Marcus, J. Chem. Phys. 84 (1986) 4894.
[32] H. Wang, M. Thoss, W.H. Miller, J. Chem. Phys. 115 (2001) 2979.
[33] M. Thoss, H. Wang, W.H. Miller, J. Chem. Phys. 115 (2001) 2991.
[34] M. Thoss, H. Wang, Chem. Phys. Lett. 358 (2002) 298.
[35] H. Wang, M. Thoss, J. Phys. Chem. A 107 (2003) 2126.
[36] J.M. Jean, R.A. Friesner, G.R. Fleming, J. Chem. Phys. 96 (1992) 5827.
[37] W.T. Pollard, R.A. Friesner, J. Chem. Phys. 100 (1994) 5054.
[38] W.T. Pollard, A.Y. Felts, R.A. Friesner, Adv. Chem. Phys. XCIII (1996) 77.
[39] D. Egorova, A. Kühl, W. Domcke, Chem. Phys. 268 (2001) 105.
[40] D. Egorova, M. Thoss, H. Wang, W. Domcke, J. Chem. Phys. 119 (2003) 2761.
[41] A.G. Redfield, Adv. Magn. Reson. 1 (1965) 1.
[42] U. Weiss, Quantum Dissipative Systems, World Scientific, Singapore, 1999.
[43] W.H. Louisell, Quantum Statistical Properties of Radiation, Wiley, New York, 1973.
[44] K. Blum, Density Matrix Theory and Applications, Plenum, New York, 1981.
[45] O. Kühn, V. May, M. Schreiber, J. Chem. Phys. 101 (1994) 10404.
[46] A.K. Felts, W.T. Pollard, R.A. Friesner, J. Phys. Chem. 99 (1995) 2929.

[47] A. Matro, J.A. Cina, J. Phys. Chem. 99 (1995) 2568.
[48] J.M. Jean, J. Chem. Phys. 104 (1996) 5638.
[49] J.M. Jean, J. Phys. Chem. A 102 (1998) 7549.
[50] D. Segal, A. Nitzan, W.B. Davis, M.R. Wasielewsky, M.A. Ratner, J. Phys. Chem. B 104 (2000) 3817.
[51] A. Kühl, W. Domcke, J. Chem. Phys. 116 (2002) 263.
[52] S. Hahn, G. Stock, J. Chem. Phys. 116 (2002) 1085.
[53] U. Kleinkathöfer, I. Kondov, M. Schreiber, Chem. Phys. 268 (2001) 121.
[54] J.M. Jean, G.R. Fleming, J. Chem. Phys. 103 (1995) 2092.
[55] S. Nakashima, Y. Nagasawa, S.K.T. Okada, M. Sato, T. Kohzuma, Chem. Phys. Lett. 331 (2000) 396.
[56] M.A. Webb, C.M. Kwong, G.R. Loppnow, J. Phys. Chem. B 101 (1997) 5062.
[57] E. Fraga, M.A. Webb, G.R. Loppnow, J. Phys. Chem. 100 (1996) 3278.
[58] M.D. Edington, W.M. Diffey, W.J. Doria, R.E. Riter, W.F. Beck, Chem. Phys. Lett. 275 (1997) 119.
[59] W. Lichten, Phys. Rev. 131 (1963) 229.
[60] F.T. Smith, Phys. Rev. 179 (1969) 111.
[61] M. Baer, Chem. Phys. 15 (1976) 49.
[62] W. Domcke, G. Stock, Adv. Chem. Phys. 100 (1997) 1.
[63] C. Kalyanaraman, D.G. Evans, J. Chem. Phys. 115 (2001) 7076.
[64] A.J. Leggett, S. Chakravarty, A.T. Dorsey, M.P.A. Fisher, A. Garg, W. Zwerger, Rev. Mod. Phys. 59 (1987) 1.
[65] R. Zwanzig, J. Chem. Phys. 33 (1960) 1338.
[66] W.A. Press, S.A. Teukolsky, W.T. Vetterling, B.P. Flannery, Numerical Recipes in Fortran—The Art of Scientific Computing, second ed., Cambridge University Press, Cambridge, 1992.
[67] B. Wolfseder, L. Seidner, G. Stock, W. Domcke, Chem. Phys. 217 (1997) 275.
[68] M. Thoss, W. Domcke, H. Wang, Chem. Phys. 119 (2003) 2761.